2022 International Conference on Unmanned Aircraft Systems (ICUAS)
Dubrovnik, Croatia. June 21-24, 2022

Design of a tactical eVTOL UAV with a Hydrogen Fuel Cell

Vasco Coelho[1], Pedro Silva[1], Paulo Sá[1], João Caetano[1], Luís Felix[1], Frederico Afonso[2] and André Marta[2]

2022 International Conference on Unmanned Aircraft Systems (ICUAS) | 978-1-6654-0593-5/22/$31.00 ©2022 IEEE | DOI: 10.1109/ICUAS54217.2022.9836046

***Abstract*— Batteries have a substantial impact on the weight of electric Unmanned Aerial Vehicles (UAVs). With fuel cells being considered a possible alternative to batteries, the present work aims to design a fixed-wing UAV with vertical take-off and landing capability and a fuel cell-based propulsion system. Building on the tactical requirements of the Portuguese Air Force, this project covers all phases of aerodynamic, structural, and propulsive design, in which Blade Element Theory, Computational Fluid Dynamics, and Finite Element Method analyses were used. The final design resulted in an inverted V-tail, 21.7kg take-off weight UAV capable of three hours of flight time, more than twice the endurance of a battery-propelled version. To further stimulate scientific knowledge sharing, the authors have made all simulations and Computational Aided Designs available to the public via repository.**

I. Introduction

Storing energy in the form of hydrogen is an area of interest for the defence sector. Recently, the European Defence Agency, through the Consultation Forum for Sustainable energy in the Defence and Security Sector, financed the RESHUB project – Defence Resilience Hub Network in Europe, which has the objective of contributing for the production of renewable energy and storing it by resorting to hydrogen [1]. Moreover, using hydrogen as energy storage is considered imperative for the political goal of zero carbon and sustainability.

Paired with the development of emerging energy sources on the aeronautical market, their implementation needs to be studied and analysed. While UAVs with internal combustion engines are preferred for long-duration missions, fossil fuels pose a serious environmental problem. In contrast, battery-powered UAVs have several advantages, including lower noise and thermal signatures, and no pollutant emissions. However, their low energy density and long charging time prevent them from being used on large-scale projects [2]. Hydrogen is another candidate to replace fossil fuel as energy source in UAVs. While hydrogen is traditionally obtained by using electricity from fossil fuels,"green hydrogen" production will tend to increase over the coming years, making hydrogen a fully zero-emission fuel source [3].

As a result, the current project details the design of a UAV that leverages the advantages of new technology, viz. H2 Fuel Cells, to develop and produce a vertical take-off and landing (VTOL) capable, 25kg Maximum Take-Off Weight (MTOW) UAV capable of carrying visible and infrared gimbaled sensors, with at least two hours of flight time.

After this brief topic overview, section II highlights the UAV conceptual design phase with its configuration definition and initial sizing. Section III details the preliminary phase of the project, with the wing and tail sizing, along with the selection of the propulsion system and drag estimation. Resorting to high-fidelity software tools, detailed analyses were conducted to support the obtained results on the aerodynamics, structure and propulsion fields, depicted in sections IV, V and VI, respectively. The major conclusions of the presented project, among with the UAV general characteristics are summarised in the final section. The files and tools created by the authors during the design process are available in a GitHub repository for consultation: `https://github.com/VascoCoelhoAero/Design-Tools`

II. Conceptual Design

A. Configuration Selection and Mission Profile

Based on the design proposal, the design process began by choosing the most suitable configuration by weighing the pros and cons of each, resorting to the Analytic Hierarchy Process (AHP) methodology [4]. Various AHP criteria were applied, from the aerodynamic and propulsion efficiency to the ease of manufacturing and maintenance, among others. Between the various configurations analysed, depicted in Fig. 1, the Lift+Cruise option was selected (Fig. 1b), a configuration with segregated propulsion systems for vertical and forward flight, thus avoiding additional rotating mechanisms and complexity. Nevertheless, having two distinct propulsion systems increases the overall weight and drag of the UAV [5].

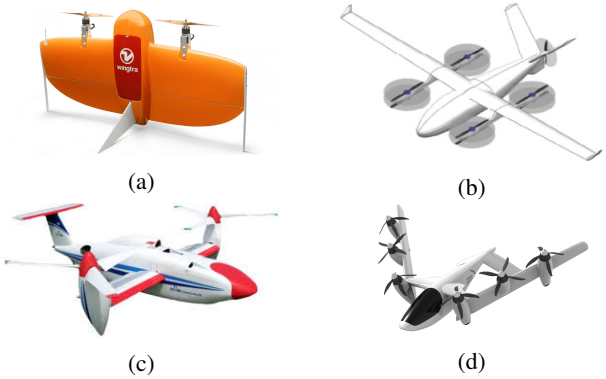

(a) (b) (c) (d)

Fig. 1: Configurations analysed with the AHP: a) Tailsitter [6] b) Lift+cruise [7] c) Tiltrotor [8] d) Transwing [9]

[1] Centro de Investigação da Academia da Força Aérea, Academia da Força Aérea, Instituto Universitário Militar, Granja do Marquês, 2715-021 Pêro Pinheiro, Portugal {vlcoelho, paasiva, pjsa, jvcaetano, lffelix}@academiafa.edu.pt

[2] IDMEC, Instituto Superior Técnico, Universidade de Lisboa, Av. Rovisco Pais 1, 1049-001 Lisboa, Portugal {frederico.afonso, andre.marta}@tecnico.ulisboa.pt

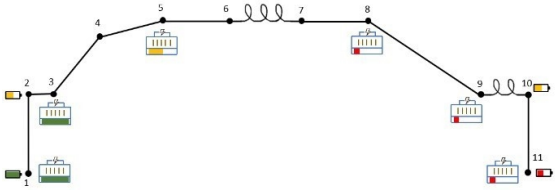

Fig. 2: UAV mission profile [5].

A main mission profile was defined in the conceptual phase, illustrated in Fig. 2. The UAV would take-off vertically (1-2) and begin its transition to forward flight (2-3). After the VTOL system is turned off, the aircraft initiates its conventional climb phase (3-5), divided into two segments, and starts the cruise/loiter mission (5-8) upon reaching an altitude of 5000 ft. At the end of the cruise segment, the aircraft glides (8-9) and performs a landing circuit (9-10), after which the VTOL propulsion system is activated again to perform the vertical descent and landing (10-11). The vertical climb and descent phases are powered by batteries dedicated to these VTOL systems with these flight segments, while the forward flight segments are powered by the hydrogen fuel cell, with the aid of an additional battery to support the required power for climb and other peak power demands.

B. Initial Sizing

The conceptual design methodology resorted to a numerical tool developed by the authors, based on references [10]–[12], together with a multi-objective optimisation algorithm to perform trade-off studies to assess the impact of some design decisions on the project. For the conceptual design, some initial parameters of the UAV regarding the airframe, motors, propellers and fuel tanks must be set, with these values being based on market studies; avionics data are based on a similar aircraft from the Air Force Academy Research Centre (CIAFA). Special care was taken when estimating C_{D_0} since the presence of the VTOL propulsion system increases the overall drag during forward flight [5].

A market study regarding possible fuel cells to be implemented in the UAV was carried out. Intelligent Energy [13] products presented the best power-to-weight ratio. The initial sizing methodology was adapted to incorporate the fixed weight of the fuel cell system, and a constraint was added to keep the required power for cruise under the fuel cell limit. The tank is selected based on the energy requirements to achieve the desired endurance.

Fig. 3: Preliminary CAD model of the UAV [5].

Fig. 4: IE-Soar 800W fuel cell system [13].

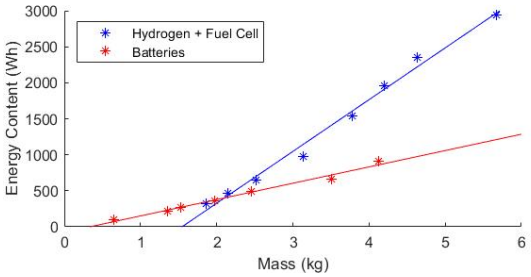

Fig. 5: Comparison between batteries and H2 system. Data sources: [15], [16]

With various combinations of fuel cell/tank tested and after the conclusion of various trade-off studies, the MTOW of the aircraft was estimated to be 21.6 kg, with its cruise flight speed at 36 kts. The aspect ratio (AR) of the wing was fixed at 11.66 with an area of 1.372 m^2. The UAV was expected to have a total flight time of 3h20, well above the two hours required. An early Computational Aided Design (CAD) model, done with OpenVSP, is visible in Fig. 3.

Regarding the fuel cell system, the IE-Soar 800 W fuel cell was selected (Fig. 4), coupled with a tank with capacity for 150g of gaseous hydrogen [14]. Energy density is a key factor in the selection of the UAV energy source. Based on [15], [16], comparing H2 fuel cell energy source against battery type configuration, Fig. 5 depicts that for energy requirements higher than 400 Wh, H2 fuel cells are preferable as it is a lighter solution. For instance, if the hydrogen system was replaced with batteries of the same weight for the current project, the total flight time would be reduced to 1h25, less than half the estimated flight time using the H2 fuel cell.

C. Flight Envelope

The flight envelope specifies the loads an aircraft structure must support during flight. This is a combination of the manoeuvrability diagram and the gust diagram. The load factor, n, is the ratio between lift and weight [11]. During the design phase of the structure, one must consider the project load factor, $n_{project}$, given by (1),

$$n_{project} = SF \cdot n_{limit}, \tag{1}$$

where SF is the safety factor used, being equal or higher than 1.5 in accordance to NATO standards [17]; n_{limit} is the limit safety factor defined in the flight envelope.

The aerodynamic forces exerted on the aircraft are maximum for manoeuvres at low altitude coupled with high

speeds, therefore, the diagram is designed for conditions at sea level. The flight envelope of the UAV only meets the requirement for the dive speed for the positive limit, reaching $n_{max} = 3.81$. Regarding the value of n_{min}, for the diving speed, $n_{min} = -1.34$ was obtained, lower (in module) than the stipulated value of -1.5 [17].

The gust diagram evaluates the impact wind gusts have on the aircraft, as these gusts change the effective angle of attack, thus influencing the lift generation [11]. For the wind gust speeds stipulated in the standard [17], the load factors are over the ones inside the flight envelope, as illustrated in Fig. 6. This phenomena is typical for small and relatively low flight speeds aircraft as the wind gusts have the same order of magnitude as the aircraft speed.

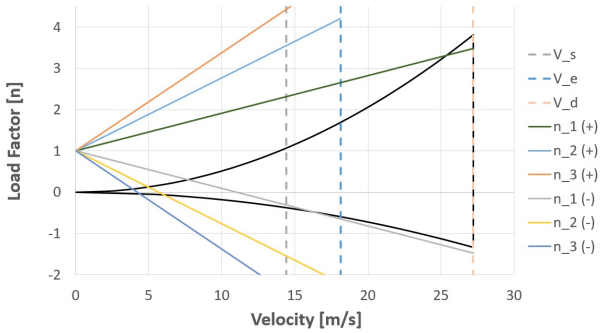

Fig. 6: Flight envelope diagram.

III. Preliminary Design

A. Wing

A boom configuration allows the division of the wing in three panels: the middle one, which goes from one boom to the other, and the tip panels outside of the booms. For simplicity and structural rigidity, the mid panel has a constant chord and no sweep. A taper ratio of 0.55 is applied to the tip panels to reduce the induced drag [18] and neither dihedral or twist are applied. For the geometry defined, the wing dimensions can be inferred, which are depicted in Fig. 7. The mean aerodynamic chord $\bar{c}$ has 0.353 m, which puts the wing Reynolds number at 3.7e5.

To define the wing airfoil, the XFOIL tool from XFLR5 [19] was used to analyse a wide range of airfoils from the University of Illinois Urbana-Champaign (UIUC) database. A 2D direct analysis was performed for a Reynolds number of 3.7e5, Mach number equal to 0.056, and e^N with N_{crit} = 9 as the transition criteria. All airfoils are normalised using 250 panels and the study was done with the angle of attack (α) varying between -15° and 25°. 3D simulations on XFLR5 for various airfoils using the wing geometry previously defined are run. Based on the aerodynamic efficiency parameter, the airfoil SG6042 was selected, which presents a $C_{L_{max}}$ = 1.46 at α_{stall} = 14° [20]. For cruise conditions, XFLR5 indicates that the wing must be set at an incidence of around 4.5° to produce the required lift for cruise,

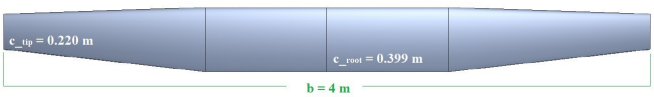

Fig. 7: Wing planform with XFLR5.

B. Main Spar

To conduct the structural analysis of the wing, a lift distribution was assumed to facilitate the design of the main spar [21]. Based on the experience of CIAFA, possible combinations of materials are presented in Tab I.

TABLE I: Mechanical properties of the materials selected for the structure.

	Carbon fibre unidirectional + epoxy	Carbon fibre bidirectional + epoxy	Airex + epoxy
Ply thickness, $[mm]$	0.222	0.190	3.00
ρ $[g/cm^3]$	1.450	1.300	0.422
E1 $[MPa]$	95070	44793	66.0
E2 $[MPa]$	9173	53193	-
$\nu 12$	0.262	0.060	0.300
G12 $[MPa]$	5000	5000	30.0
$\sigma_{US_{12}}$ $[MPa]$	49.41	90.00	1.20
Yield stress $[MPa]$	884.6	450.0	-

The preliminary design of the wing's main spar was based on the methodology developed by [22]. The selected spar cross section was identical to a wing box design, where the upper and lower caps follow part of the airfoil contour, being made of unidirectional carbon fibre (traction/compression stress), whereas the webs are made of bidirectional carbon fibre (shear stress). For the main spar geometry, it was considered a total length of 2000 mm with 40 mm of width, being the height at the root 38 mm until the location of the booms at 750 mm, decreasing linearly afterwards until it reaches 20 mm at the tip.

To estimate the ideal thickness t for the caps and webs of the main spar along its span, the bending moment at the section, the maximum yield stress for compression, tension and shear was taken into consideration [21]. A conservative approach was taken when calculating the moments of inertia by discarding the terms with thickness cubed ($t^3 \approx 0$). Additionally, a safety factor of 2 was applied for the yield stress as composite materials were used [17].

The spar was divided in 20 sections to obtain the distribution of plies. For each section, the minimum thickness was calculated with a focus on not exceeding the yield stress values. Thus, the results obtained are displayed in Tab. II with an x^y format, where x refers to the number of plies and y to the number of sections used.

Based on this information, it was then possible to analyse the stress distribution, shown in Fig. 8. The yield stress of the chosen materials is not exceeded for both caps, with the lower cap having greater stress, as expected. The multiple

TABLE II: Preliminary spar ply distribution.

Upper Cap	Lower Cap	Webs
$5^2/4^2/3^3/2^4/1^9$	$4^2/3^3/2^4/1^{11}$	$2^5/1^{15}$

discontinuity points throughout the spar represent the points where the thickness decreases and the stress instantaneously increase. For this configuration, the spar mass is 127 g.

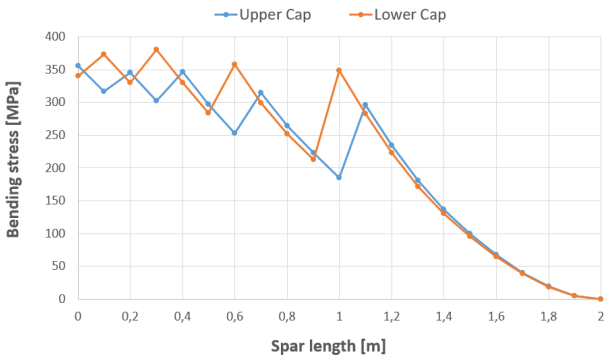

Fig. 8: Stress distribution along the preliminary spar for optimal thickness distribution.

C. Propulsion System Selection

The components of the energy and propulsion system were selected according to the output estimations and calculations from the algorithm used in the conceptual phase. At this stage, the ratios applied in the early stages are replaced by the physical components and re-iterated to check if no significant changes were made to the conceptual design. Both the batteries powering the VTOL phase and the fuel cell for peak power demands are sized. The VTOL system is selected based on the estimated thrust and power required to hover and maximum power for vertical climb, with the V605 KV210 motor (Fig. 9a) coupled with the V22x7.4 rotor being selected, as they fulfil the requirements, according to the available data from the company T-Motor [23].

For the forward propulsion system, the AT5220-A electric engine is selected (Fig. 9b). Various propellers from APC were target of a preliminary study (20x10E, 20x8E, 21x13Ea and 22x12E) by applying a Blade Element Theory (BET) methodology [24]. This methodology starts by defining the flow angles and velocities at each section. The induced angle α_i, and induced velocity w, two quantities not taken into consideration by the BET analysis, were calculated using an iterative procedure according to reference [25] and described in Fig. 10, thus adding a correction to the BET model.

The atmospheric parameters were based on the wind tunnel conditions, and the propeller's geometry was given

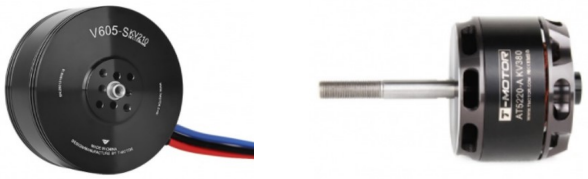

(a) (b)

Fig. 9: Electric motors: (a) V605 (vertical flight); (b) AT5220 (forward flight) [23].

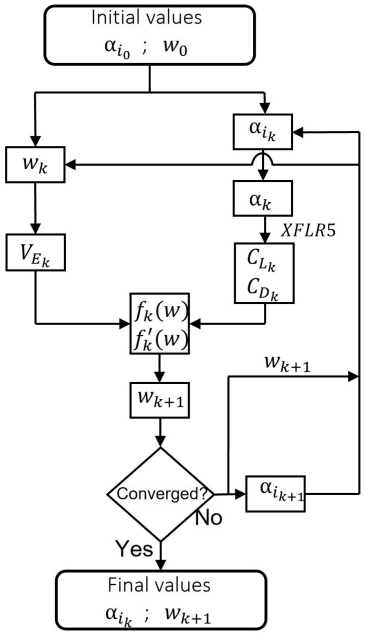

Fig. 10: Iterative procedure for obtaining the induced flow parameters in the BET methodology.

by APC. An additional adjustment was made to account for performance losses, F_{P_m}, caused by the blade tip and propeller hub [25]. Thrust and torque are computed at each section m using (2) and (3) respectively,

$$dT_m = F_{p_m}[dL\ cos(\phi_m + \alpha_{i_m}) - dD\ sin(\phi_m + \alpha_{i_m})], \quad (2)$$

$$dQ_m = F_{p_m}[dL\ sin(\phi_m + \alpha_{i_m}) + dD\ cos(\phi_m + \alpha_{i_m})]r_m. \quad (3)$$

in which ϕ represents the flow angle, the relative angle between the plane of rotation and the relative wind.

Based on the results obtained, the APC 20x10E propeller was selected as it manages to provide the thrust required during all forward flight phases, with the highest efficiency from the propellers considered.

D. Tail Geometry and CG Location

The sizing of an inverted V tail is done by considering an equivalent horizontal and vertical tail area. The equivalent horizontal tail considers the horizontal tail volume coefficient C_{HT}, which relates parameters of the tail with the wing [18]. C_{HT} is set to 0.8 and l_t to 1.5 (distance between the centre of gravity and tail aerodynamic centre) based on UAVs with a similar tail configuration, fuselage length, and the same order of magnitude for MTOW value [26]. With the total area of the V-tail being given by the sum of each equivalent tail areas [27], for a dihedral angle of 45º and for a tail AR of 5.66 when viewed from above, the tail chord has 0.255 m. For the tail airfoil, XFLR5 is used again to verify which symmetric airfoil is the most suitable for the tail, with the NACA 0008 airfoil being selected [20].

To obtain the location of the aircraft's centre of gravity (CG), a spreadsheet with the weight of all the components

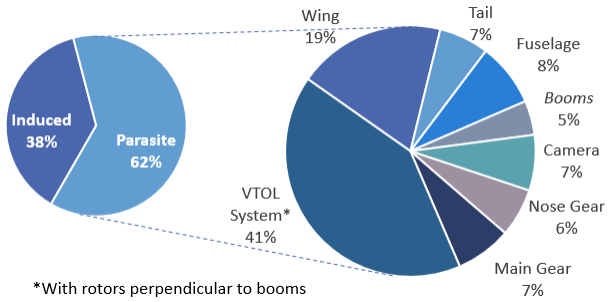

Fig. 11: Drag Build Up.

and their location was created [21]. The motors, batteries, avionics and fuel cell were arrange in the fuselage in order to facilitate their access during maintenance. For the structural parts, the weight of the structural material was estimated based the construction materials used in similar aircraft. This process indicates a MTOW of 21.77 kg, 0.8% above the one estimated in the conceptual phase, with the CG located at 875mm from the nose. A static longitudinal stability analysis on XFLR5 confirmed that the aircraft is naturally stable [20].

E. Drag Estimation

To estimated the contribution of each component to the total drag at cruise, both XFLR5 and OpenVSP softwares are used for the lift-producing surfaces and slender bodies, while semi-empirical expressions from Hoerner [28] are applied for the remaining components [20]. Fig. 11 represents the impact each structure has on the total aircraft drag at cruise, with the parasite drag being two times the induced component. It is important to note that there is a significant difference on the VTOL system contribution depending on the stopping position of the rotors during cruise, with $C_{D_{VTOL}}$ ranging between 0.00845 and 0.01690.

From the drag build-up process, the UAV yields a parasitic drag coefficient between 0.03258 and 0.04103 influenced by the rotor's position relative to the freestream, which corroborates the initial estimate of 0.04 given at the early stages of the design phase. For the induced drag component, C_{Di} = 0.0249 when considering the wing structure defined.

IV. Aerodynamic Studies

A. Assessing the CFD methodology

While XFLR5 is useful as a quick tool in the preliminary design phase, a Computational Fluid Dynamics (CFD) analysis brings more reliable results, fundamental at the detailed phase. To validate the solver properties and settings, namely the turbulence and transition models to be considered in Ansys Fluent, the CFD software selected for the external aerodynamic analysis of the UAV, a 2D analysis was performed considering the wing airfoil - SG6042, and the results compared with experimental data provided by UIUC [29] for the same airfoil. The experimental conditions are replicated in Fluent to obtain data reliable for comparison. In Fluent, a set of best practices provided by references [30] and [31] are applied, regarding the domain sizing, grid generation and solver properties. For the mesh, special care was taken in the region near the airfoil where the boundary layer is developed by introducing an inflation layer. This inflation layer must fulfil the requirements imposed by each turbulence model, namely on the dimensionless height of the first layer - y^+.

The following turbulence models were subject of comparison: the one-equation Spalart-Allmaras, the $k-\epsilon$ Realizable and Shear Stress Transport (SST) with a Low Reynolds Number (LRN) correction, both two-equation models; the $k-kl-\omega$ and SST coupled with $\gamma - Re_\theta$, two models that account for the transition phenomena. Simulations at various angles of attack were performed for comparison, with the results for $\alpha = 4°$ presented in Tab. III.

TABLE III: Comparison between experimental, XFOIL and Fluent results for $\alpha = 4°$.

	C_l	C_d	% C_l	% C_d
Experimental	0.9122	0.0091	-	-
XFOIL	0.9397	0.0082	3.01%	-9.44%
SA	0.9180	0.0158	0.64%	74.21%
$k-\epsilon$ Realizable	0.9091	0.0182	-0.33%	100.97%
SST Low Re	0.9220	0.0117	1.08%	29.18%
$k-kl-\omega$	0.9618	0.0093	5.44%	3.03%
Transition SST	0.9326	0.0093	2.24%	2.67%

These results show that both transition models feature much closer results to the experimental ones than the one and two-equation models. Both transition models managed to capture the laminar separation bubble (LSB) which occurs on the upper surface of the airfoil for positive angles of attack, inducing the transition to turbulent flow. Additionally, for negative angles of attack, a LSB is also present in the lower surface, near the leading edge of the airfoil, visible in Fig. 12. The SST transition model provided the most accurate results and a faster solution convergence than the $k-kl-\omega$, therefore confirming that the SST transition model is the most suitable for airfoil flow analysis under the LRN regime. The conclusions retrieved based on the presented results are also verified for the remaining angles of attack tested [20].

B. CFD Studies and Aircraft Performance

A CAD model of the aircraft was created to define the aerodynamic properties of the UAV. To guarantee the validity of the SST transition model ($y^+ < 1$), the first layer height of the inflation layer was defined according to the characteristic length of each airframe component. A mesh convergence study was performed, with the mesh selected having around

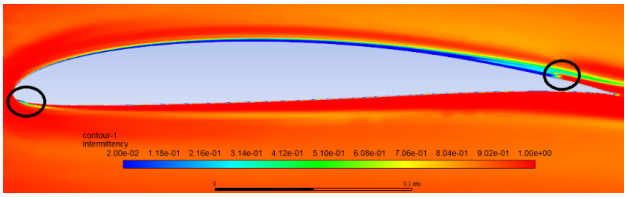

Fig. 12: Intermittency factor for $\alpha = -4°$. Black circles indicate the location of the LSB.

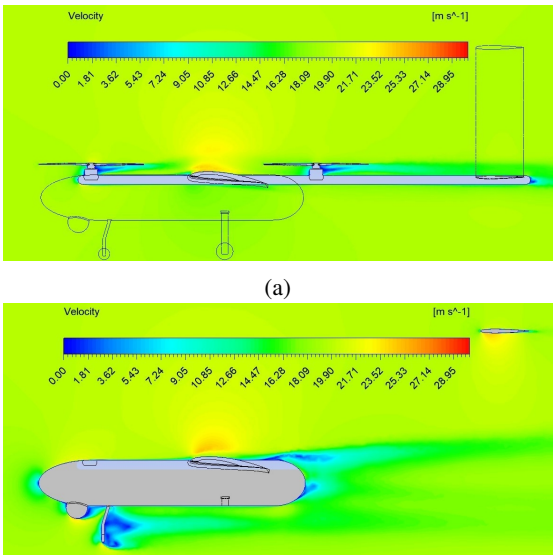

(a)

(b)

Fig. 13: Velocity contour plots of the UAV: a) at the booms plane; b) at the symmetry plane.

20M elements, with a discrepancy smaller than 2.5% in C_D when compared to the finest mesh considered [20].

Both the booms and the rotors produce a wake which influences the lift generation of the wing, as visible in Fig. 13a. Non-slender components have a big impact on the total drag, as seen in Fig. 13b. The wakes of the optical camera and the front landing gear strut significantly contribute to the form drag component. Moreover, it is visible that, on the rear of the fuselage, some detachment is occurring; in reality, the propeller creates an an active suction of the flow and prevents the boundary layer from detaching.

With the wing having an incidence of 5.75°, $\alpha = 0.15°$ manages to produce the required lift for cruise ($C_{L_{cr}}$ = 0.8269). C_D = 0.05944 for when the rotors are aligned with the flow and C_D = 0.06553 with the rotors perpendicular to the freestream. These differences directly impact the thrust required for flying and the power output required, supplied by the fuel cell. Even on the worst case, the required power output of the fuel cell is below its 800 W threshold, without making the project unfeasible. Nevertheless, the increase in the power required impacts the total flight time, reducing it from 3h25 to 3h05, an 11% decrease, thus inferring the importance of controlling the stopping position of the rotors.

To study the behaviour of the aircraft at different attitudes, simulations were performed for various angles of attack to obtain the drag polar. In this study, only the case in which the rotors are parallel to the booms is considered. The evolution of UAV lift and pitch moment coefficient with angle of attack is depicted in Fig. 14a. The lift curve slope exhibits the typical linear behaviour up to $\alpha = 4°$ and reaches a maximum value of 1.31 at 7º, after which, stall is bound to occur. The moment coefficient around the CG, confirms that the UAV is naturally stable by having the derivative $C_{M\alpha}$ negative. The angle of attack at which the moment coefficient is null is slightly higher than the one required for cruise, nevertheless, a null moment coefficient at cruise can be achieved with a slight deflection of both ruddervators [20]. Fig. 14b plots the drag curve of the aircraft, exhibiting the typical parabolic shape up to stall conditions.

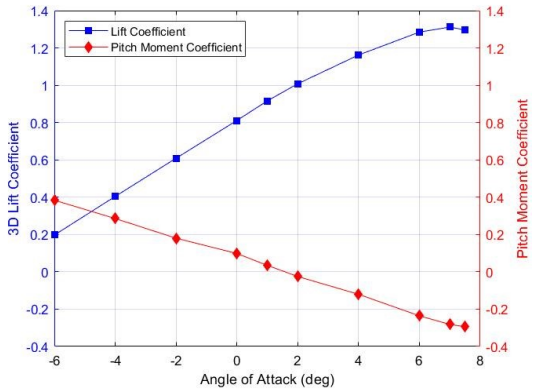

(a) CL alpha and CM alpha

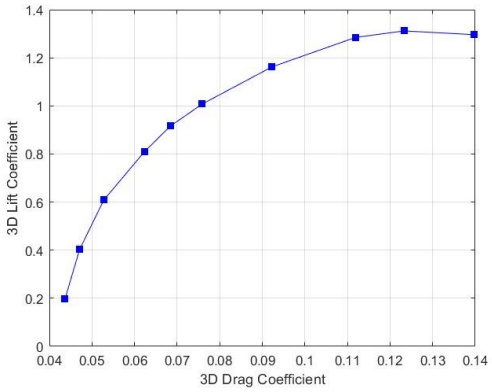

(b) Drag polar

Fig. 14: UAV aerodynamic characteristics

V. Structural Design - Wing

A. Structural Analysis of the Wing

The wing structure is composed by main spar, secondary spar and ribs. The main spar is located at the maximum thickness of the airfoil – 33.5% of the root chord, with the dimensions defined in Sec. III-B. In order to increase the torsional rigidity of the wing, the secondary spar was located at 85% of the root cord, after studying several locations ranging from 70% to 90% of the root cord. Siemens NX (Simcenter Nastran) was selected to conduct the structural analysis using Finite Element Methods (FEM).

The wing skin is composed by a stack of two plies of bidirectional carbon fibre, one at $45°$ and the other at $-45°$ relative to the wing spar axis. For the main spar, a parametric study was conducted to choose the best configuration. Since the geometry is different from the preliminary case, five new different configurations were simulated, displayed in Tab. IV. The lift distribution is identical to the one used

TABLE IV: Main spar ply distribution.

	Upper Cap	Lower Cap	Webs
Config 1	$5^2/4^2/3^3/2^4/1^9$	$4^2/3^3/2^4/1^{11}$	$2^5/1^{15}$
Config 2	$6^2/5^2/4^3/3^4/2^9$	$5^2/4^3/3^4/2^{11}$	$2^5/1^{15}$
Config 3	$4^2/3^3/2^4/1^{11}$	$5^2/4^2/3^3/2^4/1^9$	$2^5/1^{15}$
Config 4	$5^2/4^2/3^3/2^4/1^9$	$5^1/4^1/3^3/2^4/1^{11}$	$2^5/1^{15}$
Config 5	$5^1/4^3/3^3/2^4/1^9$	$5^1/4^2/3^3/2^4/1^{10}$	$2^5/1^{15}$

in the preliminary case, with the mesh having 5 mm squared elements with four nodes each.

Tab. V display the results obtained. Only configurations 2 and 5 are within the yield stress requirements. Configuration 5 was selected as it is lighter, with the unidirectional carbon fibre being aligned with the wing span direction.

The secondary spar has an I-beam structure with the flanges having two plies of unidirectional carbon fibre aligned with the spar, and the web having a sandwich structure of Airex foam and bidirectional fibre at $-45°$. The seven ribs incorporated in the wing structure have the same configuration: one ply of bidirectional carbon fibre at $45°$, followed by a ply of unidirectional carbon fibre at $90°$ and finally, another ply of bidirectional carbon fibre at $-45°$. For this case, the principal direction of stress is the direction of the wing profile thickness.

This wing configuration has a total structural weight of 1.19 kg, with 85% of this weight being referred to the wing skin. To conduct a structural analysis of the wing at cruise conditions, the aerodynamic loads provided by the CFD simulations previously described were applied. The pressure field given at the wing surface was applied in the Siemens NX FEM software. As the cruise condition is far from the structural limit, a factor of $n = 6$ (rounding up the 3.81×1.5 value for n) was considered [17]. The pressure field applied is visible in Fig. 16.

A mesh convergence study was performed to obtain the most accurate results within the available computational resources. Von Mises stress were computed in a section between 100 and 300 mm of the main spar upper flange (Fig. 17). For a mesh with elements smaller than $4\ mm$, the

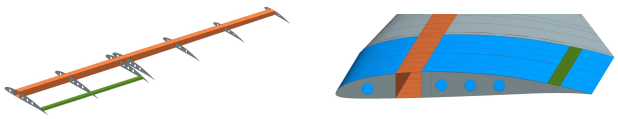

(a) (b)

Fig. 15: Wing half CAD model. Structure: main spar (orange), secondary spar (green), ribs (grey). Skin (blue).

TABLE V: Displacement and stress maximum values for each configuration.

	Mass $[g]$	Displacement $[mm]$	Stress $[MPa]$
Config 1	127	273	485.58
Config 2	178	196	372.14
Config 3	127	273	485.58
Config 4	128	269	484.13
Config 5	132	259	423.39

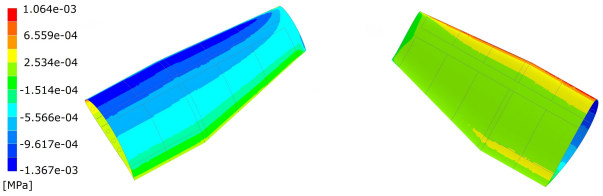

(a) (b)

Fig. 16: Pressure distribution. (a) Upper surface; (b) Lower surface.

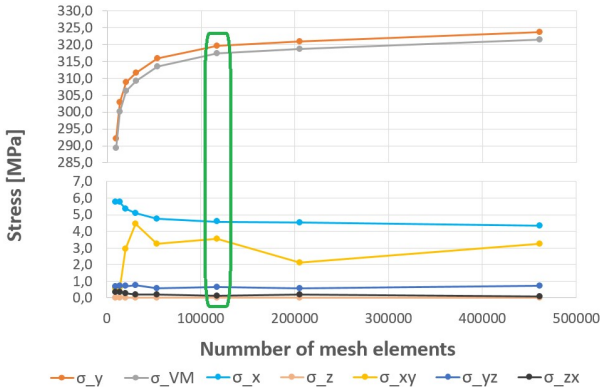

Fig. 17: Structural mesh convergence study

stress variation is negligible, thus considering the mesh is convergent.

B. Structural Results

To analyse the wing structure, the tip displacement and the Von Mises stress distribution were computed for the pressure field represented in Fig. 16. The maximum displacement at the tip was $168.3\ mm$. Von Mises stress distribution is shown in Fig. 18. The maximum stress value registered at any unidirectional ply was $421.7\ MPa$, whereas, for bidirectional plies was 217.4. Both values are lower than the material limits corrected with the safety factor (Tab. I). Static analysis results shows that the wing structure is capable of withstand the expected aerodynamic loads.

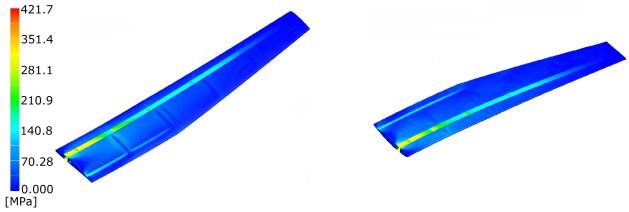

(a) (b)

Fig. 18: Wing *Von Mises* stress. (a) Upper surface; (b) Lower surface.

VI. Propulsion System Analysis

A. Computational Fluid Dynamics

To validate the data given by the suppliers and the results from the BET analysis, both propulsion systems were subject

Fig. 19: CAD model of the V22x7.4R propeller.

Fig. 20: CAD model of the APC 20x10E propeller.

to CFD simulations. The forward flight propeller was modelled using the data provided by APC regarding the geometry of various sections. For the vertical flight propeller, the information regarding the rotor's geometry was unavailable. To create a CAD model of the rotor, a negative cast in plaster of the rotor was made, followed by the creation of a positive mold in wax. After that, the mold is split into portions, and images of the airfoil at various sections are taken. The points of each profile are obtained using image editing software and then transferred into a CAD software, resulting in the model [24]. The CAD models of the V22x7.4 and APC20x10E propellers are shown in Fig. 19 and 20, respectively.

Following this process, the computational domain was defined as illustrated in Fig. 21. The multiple reference frame methodology was considered in this study [24].

The mesh is generally unstructured, except at the inflation layer defined in the region around the airfoil, where the boundary layer is developed. The value of y^+ = 70 was defined for all sections of the blade to store all the information within the boundary layer. This decision was taken due to the change of various factors along the blade, therefore an intermediate y^+ value was chosen so that the variable values during a CFD analysis did not surpass the limits of the $k-\epsilon$ model ($30 < y^+ < 300$), the turbulence model chosen which is commonly used in rotational flows [31].

After defining the local refinements in the computational domain, a mesh convergence analysis was performed, with reference to the size of the elements in each region. Thrust and torque were the variables of interest for these studies. The number of elements per mesh, the value of the variables of interest, and the respective error related to the finest mesh for the 20x10E propeller are found in Tab. VI. A threshold of 5 % for error was defined as acceptable, hence, the mesh with 975k elements was selected.

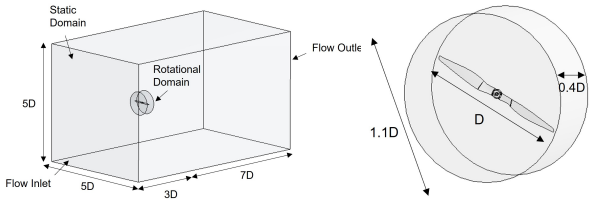

(a) (b)

Fig. 21: Computational domain. (a) Static domain and dimensions; (b) Rotational domain and dimensions.

TABLE VI: APC 20x10E propeller mesh convergence study.

Nº elements	Thrust [N]	Error [%]	Torque [Nm]	Error [%]
569559	17.07	-28.32	1.149	-10.98
974620	19.49	-18.13	1.225	-5.040
2288415	21.98	-7.665	1.272	-1.464
4457592	22.69	-4.715	1.277	-1.077
11430631	23.81	–	1.290	–

B. Wind Tunnel Analysis

The APC 20x10E propeller was analysed at cruise speed in the wind tunnel, and the rotor V22x7.4 at stationary conditions to recreate the hover segment. The atmospheric conditions in the tunnel are presented in Tab. VII, which were also applied in the previous analysis.

The experimental setup consists of a Lorenz M-2366 force and torque sensor connected to a Microlink 751 data gathering device, and then to a computer for data reading. The motor is installed next to the force and torque sensor in accordance with the test to be performed. Attached to the ESC, a Hitec HFP-25 digital servo programmer was used to control the rotations. The methods used in [32] were followed to visualise the information provided by the programmer. The motor, ESC, sensor, propeller, and three-phase connection are part of the test bench, and are visible in Fig. 22.

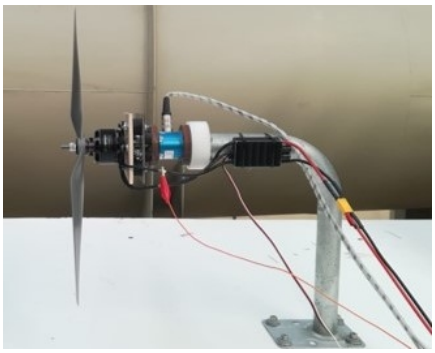

Fig. 22: Wind tunnel test bench

The results of the 20x10E and V22x7.4 propellers in the wind tunnel demonstrate that the 20x10E propeller is able to produce the required thrust for the cruise and climb segments, operating at 5000 and 6000 RPM, respectively. For the VTOL system, hover can be achieved at around 5000 RPM. The standard deviation, which is under one Newton for all the spectrum of RPM tested, indicates that the samples and data retrieved are acceptable for future comparison. The experimental results serve as reference for comparison with the computational analysis.

TABLE VII: Wind tunnel Conditions.

Wind Tunnel Conditions	
Temperature	23.2 ºC
Static Pressure	103.9 kPa
Dynamic Pressure	234 Pa
Density	1.222 kg/m^3
Flow Velocity	19.57 m/s
Dynamic Viscosity	1.829E-5 Ns/m^2

C. Interpreting the results from each method

Fig. 23 compares the data acquired during the analysis of the 20x10E propeller and the V22x7.4 rotor. Except for the 4500 RPM, differences of less than 10% in the thrust, torque, and efficiency parameters were found when comparing experimental and CFD results for the 20x10E propeller, which represents an acceptable range of values [24]. In terms of the computational analysis, the presented methodology is capable of reliably predicting the studied parameters for greater rotations. For low rotations, the Reynolds number is lower, reducing the y^+ values at low rotations for the same mesh. Once this variable goes below the minimum imposed by the turbulence model, it is projected that the relative difference will grow as the RPM are reduced [24].

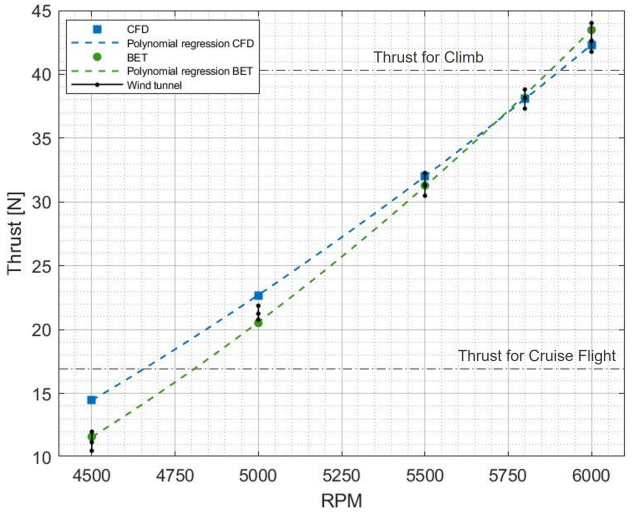

(a)

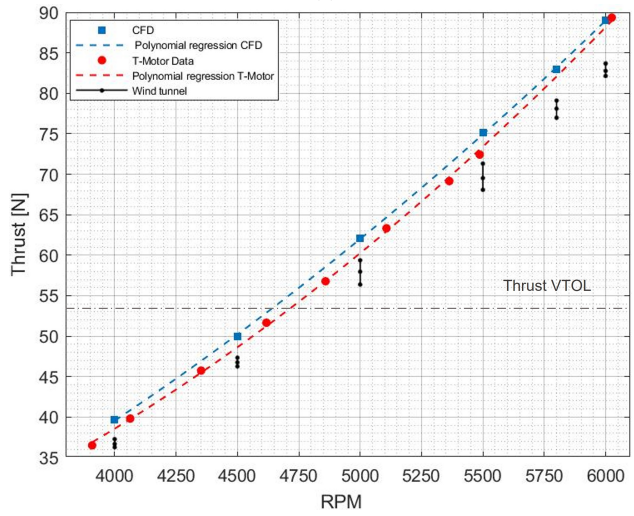

(b)

Fig. 23: Thrust representation at different RPM: (a) 20x10E Propeller (b) V22x7.4 Rotor.

According to the results of the BET study, the approach used to create an initial prediction of thrust values is valid, as the values calculated are within the range of the wind tunnel experimental results. This conclusions infers that the BET methodology with the corrections considered is valid for an early estimate of the propeller's performance.

When comparing the CFD values to the experimental wind tunnel results for the rotor V22x7.4 (Fig. 23.b), the CFD values overestimate the thrust created by the rotor. There is a systemic inaccuracy of about 7-8%, which can have multiple justifications, such as slight differences between the rotors actual geometry and model, or a miss-calibration of the sensors at the test bench. Despite the fact that the torque parameter has a significant error (>10%), the methodology used throughout the process, from modelling to CFD simulations, is regarded appropriate as the thrust error and the Figure of Merit (an indicator of the rotor's efficiency) have deviations below 10%. As a result, should wind tunnel testing not be feasible, CFD analysis is possible, bearing in mind the possible 10% difference in the results. This is of particular importance for researches which cannot perform wind tunnel testing.

The value of the efficiency parameter acquired in the experimental and computational analysis is estimated to be around 66%. Based on the authors' examination of the propeller efficiency in the pusher-type configuration [33], it is possible to verify that for a d_{fus}/D ratio of approximately 0.47, the efficiency of the pusher and tractor designs exhibit roughly the same value. In this context, and given the 0.24 m value of the fuselage diameter, d, and the selection of the 20x10E propeller, it can be concluded that the selected propeller efficiency in the pusher configuration is around 66%. As a result, it can be determined that the propulsive system chosen fits the project criteria and is capable of ensuring cruise flight, conventional climb, and VTOL.

With the detail design phase concluded, the UAV characteristics are updated and the final parameters are present in Tab. VIII.

TABLE VIII: UAV general characteristics.

Weights		Wing	
MTOW	21.77 kg	Aspect Ratio	11.66
Structural	6.11 kg	Area	1.372 m^2
Propulsion	2.62 kg	Span	4 m
H2 System	4.48 kg	Mean Chord	0.353 m
Energy	2.91 kg	Airfoil	SG6042
Tail		**VTOL Prop System**	
Total Area	0.516 m^2	Motor	V605 (x4)
Dihedral	45°	Rotor	22x7.4 (x4)
Arm	1.5 m	P Hover[1]	858.1 W
Chord	0.255 m	P max[1]	3183 W
Airfoil	NACA0008	RPM Hover	4734
Forward Prop System		**Performance**	
Motor	AT5220	Stall Speed	28 kts
Propeller	APC 20x10	Max ceiling	10000ft
η_{pr}	0.66	Cruise Speed	38 kts
P cruise[2]	654 - 756 W	Climb Speed	36 kts
P climb[2]	1387 - 1471 W	Climb Angle	6.2°
T cruise	16.3 - 19.2 N	Cruise Altitude	5000ft
T climb	39.2 - 41.9 N	Flight time	3h05 - 3h25

[1]Power per motor/rotor set

[2]Includes motor required power, motor and ESC efficiencies, and avionics and camera power consumption

VII. Conclusions

The present work focused on designing an UAV with VTOL capabilities and having a hydrogen fuel cell as energy source for cruise. A Lift+Cruise configuration was selected with early studies confirming the advantages of resorting to hydrogen instead of batteries, as the battery solution presented less than half the endurance.

To support the results obtained in the conceptual and preliminary design, detailed studies were performed, using high-fidelity computational tools. For the aerodynamic area, the SST Transition model was verified and applied, with the complete aircraft simulation being able to predict the aerodynamic properties and performance of the UAV. Structural analysis of the wing demonstrated that the structure idealised is able to withstand the limit loads of the UAV. The CFD and wind tunnel tests for the propulsion system have deviations smaller than 10% when compared to the BET methodology, thus confirming this method is viable at the preliminary design phase.

The preliminary computational tools used throughout this project are available for consultation in a repository, allowing for third party to use them on similar design cases.

Some topics may be further explored to improve the UAV performance, such as controlling the stopping position of the rotors to reduce drag at cruise or idealising a different wing structure which would fulfil the structural requirements while being lighter. Moreover, studies on other areas such as flight control and energy management of the fuel cell should be developed to achieve the goal of manufacturing a prototype.

ACKNOWLEDGMENT

F.A acknowledges Fundação para a Ciência e a Tecnologia (FCT), through IDMEC, under LAETA, project UIDB/50022/2020

References

[1] SiEnE, "Reshub project," 2022, Accessed: 20/01/2022. [Online]. Available: https://siene.teces.si/en/reshub-project/

[2] Airbus, "How hydrogen could be a game-changer for future aircraft," 2020, Accessed: 28/04/2021. [Online]. Available: https://www.airbus.com/newsroom/stories/Is-this-the-next-clean-energy-to-power-aviation.html

[3] ——, "Hydrogen in aviation: how close is it?" 2020, Accessed: 28/04/2021. [Online]. Available: https://www.airbus.com/newsroom/stories/hydrogen-aviation-understanding-challenges-to-widespread-adoption.html

[4] T. L. Saaty and L. G. Vargas, *Models, Methods, Concepts & Applications of the Analytic Hierarchy Process*, 2nd ed., ser. International Series in Operations Research & Management Science. Springer, 2012, ISBN: 978-1-4614-3597-6.

[5] B. Alves, V. Coelho, P. Silva, A. Marta, F. Afonso, P. Sá, L. Félix, and J. Caetano, "Design of a hydrogen powered small electric fixed-wing uav with vtol capability," in *International Conference on Multidisciplinary Design Optimization of Aerospace Systems*, A. C. Marta and A. Suleman, Eds., ECCOMAS. Lisbon, Portugal: Aerobest 2021, July 2021, pp. 290–304, ISBN: 978-989-99424-8-6.

[6] Wingtra, "Tailsitters vs. quadplanes – why a VTOL tailsitter is the best surveying drone for your mapping missions," https://wingtra.com/, November 2018.

[7] D. F. Finger, C. Braun, and C. Bil, "A review of configuration design for distributed propulsion transitioning VTOL aircraft," in *Asia-Pacific International Symposium on Aerospace Technology (APISAT)*, Seoul, Korea, Oct. 2017.

[8] S. Park, J. Bae, Y. Kim, and S. Kim, "Fault tolerant flight control system for the tilt-rotor uav," *Journal of the Franklin Institute*, vol. 350, no. 9, pp. 2535–2559, 2013.

[9] sUAS News, "Transwing – a revolutionary VTOL," https://www.suasnews.com/2019/03/transwing-a-revolutionary-vtol/, Mar. 2019.

[10] T. C. Corke, *Design of Aircraft*. New Jersey: Pearson Education, Inc., 2003, ISBN:0-13-089234-3.

[11] D. P. Raymer, *Aircraft Design: A Conceptual Approach*. American Institute of Aeronautics and Astronautics, Inc, 1992, ISBN:0-930403-51-7.

[12] J. Gundlach, *Designing Unmanned Aircraft Systems: A Comprehensive Approach*. American Institute of Aeronautics and Astronautics, Inc, 2012, ISBN:978-1-60086-843-6.

[13] Intelligent Energy, "Our uav products," Charnwood Building, Holywell Park, Ashby Road, 2021, Accessed: 17/06/2021. [Online]. Available: https://www.intelligent-energy.com/our-products/uavs/

[14] *Intelligent Energy*, *Guide to Cylinder Options for UAV Applications*, Charnwood Building, Holywell Park, Ashby Road, 2020.

[15] ——, *Guide to Cylinder Options for UAV Applications*, Charnwood Building, Holywell Park, Ashby Road, 2020.

[16] G. A. Store, "Tattu gensace - uav lipo batteries," http://https://www.gensace.de/uav-lipo, 2021.

[17] NATO, "Light unmanned aircraft systems airworthiness requirements - NATO STANDARD AEP-83," Allied Engineering Publication, 2014, 1-8 UL.5.

[18] M. H. Sadrey, *Aircraft Design - A Systems Engineering Approach*. John Wiley & Sons, Ltd, 2013, ISBN:978-1-119-95340-1.

[19] A. Deperrois, *XFLR5 - Analysis of foils and wings operating at low Reynolds numbers*, 2009.

[20] V. Coelho, "Aerodynamic detailed design of an unmanned aerial vehicle with vtol capabilities," Master's thesis, Academia da Força Aérea, Sintra, Portugal, 2021.

[21] P. Sá, "Projeto estrutural detalhado de um uav com fuel cell," Master's thesis, Academia da Força Aérea, 2021.

[22] M. Hollmann, *Composite Aircraft Design*, 5th ed. Aircraft Designs, INC., 2003, ISBN:978-1893639003.

[23] T-Motor, "T-motor website," 2021, Accessed: 11/06/2021. [Online]. Available: https://store-en.tmotor.com/

[24] P. Silva, "Design detalhado de um uav com fuel cell, foco em aerodinâmica e desempenho," Master's thesis, Academia da Força Aérea, 2021.

[25] S. Gudmundsson, *General Aviation Aircraft Design: Applied Methods and Procedures*. Elsevier, 2014, ISBN: 978-0-12-397308-5.

[26] D. Coelho, "Conceptualization and application of unmanned aerial vehicles design methodology," Master's thesis, Instituto Superior Técnico, 2019.

[27] P. E. Pursee and J. P. Campbell, "Experimental verification of a simplified vee tail theory and analysis of available data on complete models with vee tails," NACA, UNT Libraries Government Documents Department, Tech. Rep. 823, 1944.

[28] S. F. Hoerner, *Fluid-dynamic drag*. Hoerner fluid dynamics, 1965.

[29] M. Selig, *Summary of low speed airfoil data Vol. 3*. SoarTech Publications, 1997.

[30] R. Veríssimo, "Best practice guidelines in cfd external aerodynamics: Applied to unmanned aerial vehicles at cruise conditions," Master's thesis, Academia da Força Aérea, 2016.

[31] Ansys Inc., *Ansys Fluent User's Guide, Release 15.0*, 11 2013.

[32] P. Mendes, "Design of a fixed-wing tilt-rotor quadcopter class i mini unmanned aircraft - propulsion system design and prototype manufacturings," Master's thesis, Academia da Força Aérea, 2021.

[33] J. Roskam and C.-T. E. Lan, *Airplane Aerodynamics and Performance*. Design, Analysis and Research Corporation, 1997, ISBN: 978-1884885440.